Wireless Power Transfer

ARTICLE

Open Access

https://doi.org/10.48130/wpt-0026-0018

Wireless Power Transfer **2026**, 13: e030

Research on multi-coil wireless charging efficiency optimization system for unmanned aerial vehicles: based on input control and PSO algorithm

Hongyu Li[1], Yu Liu[1], Shui Pang[2], Jiayi Xu[2], Yuhang Yang[1], Chenxi Li[1], Yu Zhang[1*] and Shaobo Yang[1]

[1] *Shandong University of Science and Technology, Qingdao 266590, China*

[2] *Tianjin University, Tianjin 300072, China*

* Correspondence: skd994496@sdust.edu.cn (Zhang Y)

Abstract

To address the significant impact of positional deviation during unmanned aerial vehicle (UAV) landing on the power transfer efficiency of wireless power transfer (WPT) systems, this paper proposes a Multi-Transmitter Array Wireless Power Transfer (MTA-WPT) system. A theoretical analysis is conducted on the influence of input voltage amplitude and phase on receiver power and efficiency under different mutual inductance matrices. Through simulation, a topology with five transmitting coils and one receiving coil is ultimately selected. By introducing a Particle Swarm Optimization (PSO) algorithm to adjust the input voltage amplitude and phase, the system achieves improved charging efficiency while maintaining stable power output during the horizontal translation of the receiver above the coil array. Experimental validation demonstrates that when the UAV battery is charged at a power level of approximately 30 W, the system efficiency increases by up to 10.16 % compared to operation without algorithm control. The proposed solution effectively mitigates charging instability caused by inaccurate UAV landing, providing reliable wireless charging support for UAVs under positional offset.

Keywords: Wireless Power Transfer, Unmanned Aerial Vehicle (UAV), Multiple Transmitting (Tx) Coils, Particle Swarm Optimization

Citation: Li H, Liu Y, Pang S, Xu J, Yang Y, et al. 2026. Research on multi-coil wireless charging efficiency optimization system for unmanned aerial vehicles: based on input control and PSO algorithm. *Wireless Power Transfer* 13: e030 https://doi.org/10.48130/wpt-0026-0018

Introduction

Wireless power transfer (WPT), as a contactless power delivery method, offers advantages such as convenience, safety, reliability, and environmental adaptability[1,2]. It reduces risks associated with physical connectors, such as wear, sparking, and explosion, thereby providing essential technological support for the continuous autonomous operation of devices. WPT shows broad application prospects in various fields, including electric vehicles[3–5], power supply and monitoring for underwater equipment[6–8], and wireless charging for unmanned systems such as UAV[9,10].

Among these applications, autonomous charging for unmanned aerial vehicles (UAVs) is a particularly valuable research direction. In long-duration missions, endurance is a key bottleneck for UAV performance. However, during autonomous landing, factors such as navigation inaccuracy and environmental disturbances (e.g., wind) often cause deviation between the actual landing position and the preset charging platform center. This misalignment significantly affects the relative positioning and coupling between transmitter and receiver coils, thereby degrading the system's power transfer efficiency[11].

To enhance the misalignment tolerance of WPT systems, several approaches have been studied, including different coupler structures[12,13], improving landing accuracy[14], implementing primary-side and secondary-side control[15,16], adopting different compensation topologies[17], and applying impedance matching techniques[18]. While these methods partially improve tolerance to misalignment, they still struggle to meet the charging requirements of UAVs over large, arbitrary landing areas. In recent years, multi-transmitter coil array systems have attracted increasing research attention. Such structures can significantly expand the effective charging area and improve anti-misalignment performance[19,20].

To address the instability in power and efficiency caused by positional offset in multi-transmitter array systems, various methods have been proposed, focusing on coil array geometry, suppression of cross-coupling, and control of system inputs. In terms of coil array structures, these can be categorized into 2-D planar arrays[21] and 3-D orthogonal arrays[22]. In 3-D orthogonal structures, output control is typically achieved by regulating the amplitude and phase of currents. However, 2-D planar arrays offer greater scalability. In planar parallel coil arrangements, magnetic field cancellation may occur in certain regions. To mitigate this, improvements have been made to both primary and secondary coil designs: primary coils can be stacked[23], while secondary coils may adopt asymmetric structures that encompass multiple primary coils[24].

In multi-coil systems, cross-coupling among transmitting coils increases reactive power and reduces overall system efficiency. For two-coil systems, cross-coupling can be minimized by overlapping the coils[25]. For systems with more than two coils, variable reactance methods may be employed to suppress cross-coupling[26].

System power and efficiency can be controlled from either the primary or secondary side. However, to extend UAV flight time, minimizing weight on the secondary side is preferred. Therefore, in this work, system performance is regulated by controlling the input—specifically the amplitude, phase, and frequency of the excitation. For a two-transmitter (Tx) coil system with adjustable current amplitude, the optimal current ratio between the two Tx coils is equal to the ratio of their coupling coefficients with the receiver[27]. By analyzing the phase effect on power via magnetic flux angle measurements and using a BP neural network to learn the phase–current relationship of the magnetic flux, the influence of phase on power has been validated[28]. Simultaneous amplitude and phase control in multi-coil arrays can enhance the system's transmission efficiency coefficient[29]. By predefining the frequency

© The Author(s)

and phase of Tx coil currents and employing suitable dual-frequency quad-phase combinations, multi-Tx WPT systems can provide full positional and rotational charging freedom to the receiving (Rx) coil[30].

Thus, output power control is essential in WPT systems. While operating frequency is usually fixed, controlling the amplitude and phase of the input voltage is relatively straightforward. To compensate for efficiency losses due to receiver displacement, this paper proposes a multiple-transmitter-array WPT system. By regulating the amplitude and phase of the input voltage, the system achieves constant-power charging with high efficiency even when the UAV is offset from the intended landing position.

The paper is organized as follows. The Materials and methods section models and analyzes the MTA-WPT system, focusing on the circuit model of a five-coil system. The Multi-input coil amplitude and phase optimization algorithm section presents an optimization algorithm for the amplitude and phase of the multiple input coils using a particle swarm optimization (PSO) approach. The Results section provides experimental and simulation analyses of the optimal efficiency search algorithm for the MTA-WPT system, including prototype construction and testing, constant-current charging experiments, and efficiency comparisons under lateral and diagonal offsets. Finally, the Conclusions section summarizes the main findings.

Materials and methods

Modeling and analysis of the MTA-WPT system

Circuit model

To achieve constant current charging for the UAV during the charging process, the system adopts an LCC-P compensation topology, which exhibits near-constant-current characteristics on the load side. Figure 1 shows the schematic diagram of the MTA-WPT system. The designed MTA-WPT system employs five transmitting coils and one receiving coil. All transmitting coils are powered by a single source and share identical configurations, but each has a dedicated inverter and compensation circuit. Input voltage amplitude and phase control for the multi-transmitter system is realized by modulating the PWM waveform fed to each inverter.

Figure 2 illustrates the circuit model of the system. Figure 3 Structure diagram of the unmanned aerial vehicle charging system. L_{rn}, C_{rn}, and C_{pn} represent the compensation inductance and capacitance of the nth input coil; L_{pn}, L_s denote the self-inductances of the nth transmitter coil and the receiver coil; C_s is the compensation capacitance at the receiver side; R_{rn}, R_{pn}, and R_s are the parasitic resistances of the nth input compensation inductor, the nth transmitter coil, and the receiver coil, respectively; $M_{ij}(1 \le i, j \le n)$ is the mutual inductance between coil i and coil j; M_i $(1 \le i \le n)$ represents the mutual inductance between coils i and the receiving coil; R_l is the load resistance. When the rectifier-filter circuit operates under ideal conditions, an equivalent resistance $R_L = \frac{8}{\pi^2} R_l$ exists. In this MTA-WPT system, multiple inputs lead to cross-coupling, so mutual inductances among input coils must be considered. Applying Kirchhoff's Voltage Law (KVL), where j denotes the imaginary unit and ω represents the system's operating angular frequency, the circuit equations for the LCC-P system are:

$$\begin{cases} Uin_1 == I_1(j\omega L_{r1} + R_{r1}) + I_{p12}\dfrac{1}{j\omega C_{r1}} \\ I_1 = I_{p11} + I_{p12} \\ \dfrac{I_{p12}}{j\omega C_{r1}} = I_{p11}\left(j\omega L_{p1} + \dfrac{1}{j\omega C_{p1}} + R_{p1}\right) - j\omega(M_1 I_s + M_{12} I_{p21} + \cdots + M_{1n} I_{n1}) \\ Uin_2 == I_2(j\omega L_{r2} + R_{r2}) + I_{p22}\dfrac{1}{j\omega C_{r2}} \\ I_2 = I_{p21} + I_{p22} \\ \dfrac{I_{p22}}{j\omega C_{r2}} = I_{p21}\left(j\omega L_{p2} + \dfrac{1}{j\omega C_{p2}} + R_{p2}\right) - j\omega(M_{21} I_{11} + M_2 I_s + \cdots + M_{2n} I_{n1}) \\ \cdots \\ Uin_n == I_n(j\omega L_{rn} + R_{rn}) + I_{pn2}\dfrac{1}{j\omega C_{n1}} \\ I_n = I_{pn1} + I_{pn2} \\ \dfrac{I_{pn2}}{j\omega C_{rn}} = I_{pn1}\left(j\omega L_{pn} + \dfrac{1}{j\omega C_{pn}} + R_{pn}\right) - j\omega(M_{n1} I_{11} + M_{n2} I_{p21} + \cdots + M_n I_s) \\ \dfrac{I_s}{Z_S} = j\omega(M_1 I_{11} + M_2 I_{p21} + \cdots M_n I_{n1}) \end{cases} \tag{1}$$

where, I_n, I_{n1}, and I_{n2} represent the system's input current, the current in the input coil; and the current of the input resonant capacitor C_{rn}; I_s is the receiver coil current; Z_S is the equivalent impedance at the receiver; Z_S is derived as shown in:

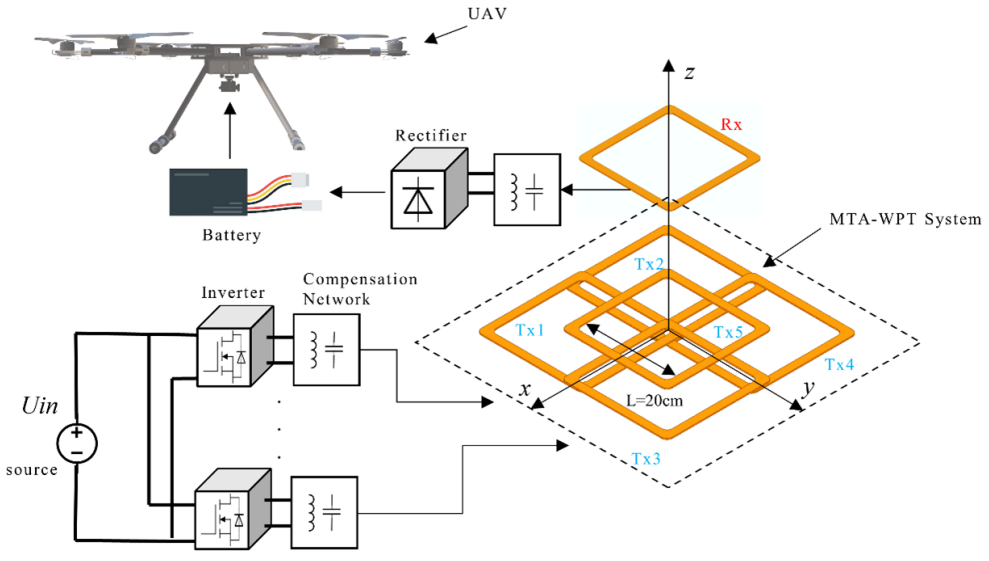


Fig. 1 Schematic diagram of the MTA-WPT system.

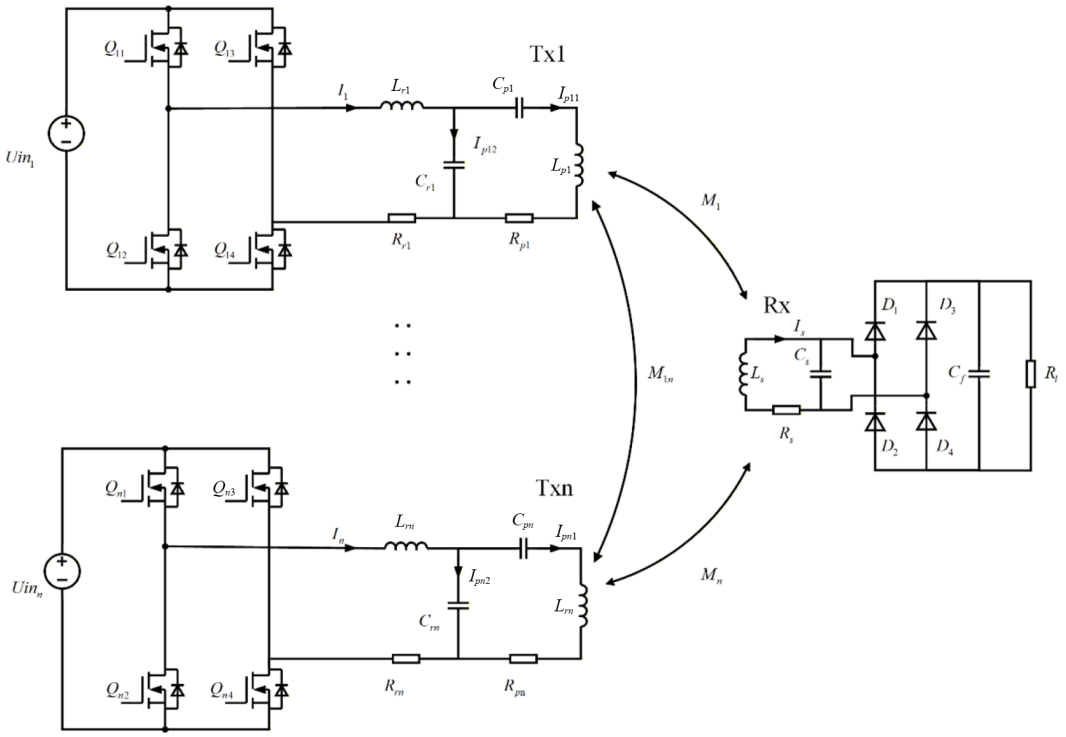


Fig. 2 MTA-WPT system circuit model.

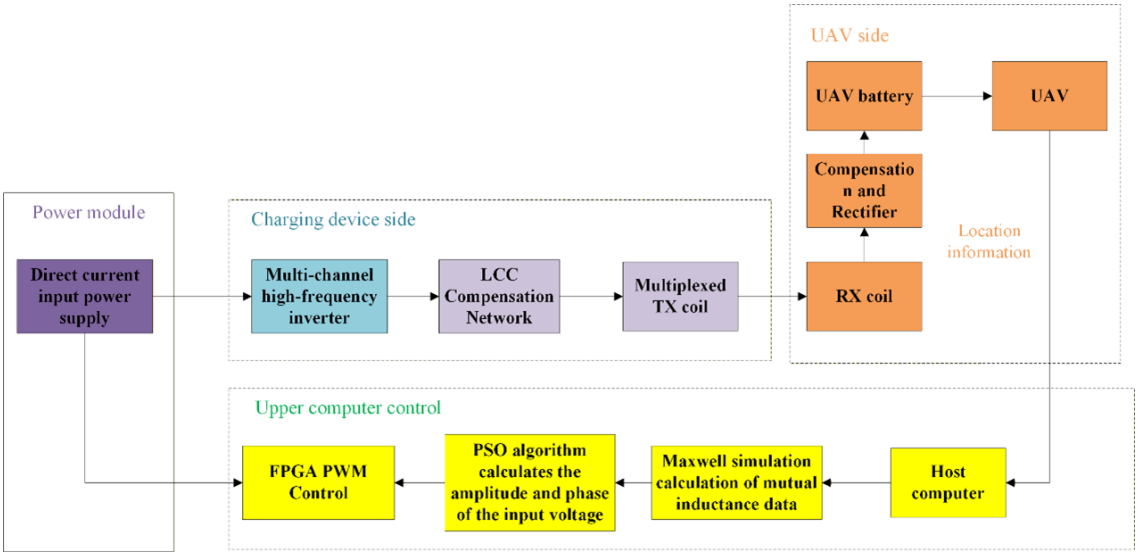


Fig. 3 Structure diagram of unmanned aerial vehicle charging system.

$$\begin{cases} Z_{cs} = \dfrac{1}{j\omega C_s} \\ Z_p = \dfrac{1}{\left(\dfrac{1}{Z_{cs}} + \dfrac{1}{R_L}\right)} \\ Z_S = j\omega L_s + Z_p + R_s \end{cases} \tag{2}$$

When the LCC-P compensation operates in resonance mode, its compensation network parameters satisfy:

$$\begin{cases} j\omega L_{rn} = -\dfrac{1}{j\omega C_{rn}} \\ j\omega(L_{pn} - L_{rn}) = -\dfrac{1}{j\omega C_{pn}} \\ j\omega L_s = -\dfrac{1}{j\omega C_s} \end{cases} \tag{3}$$

In efficiency analysis, parasitic resistances of all components affect system performance. However, measured results show that the parasitic resistance of compensation capacitors is very small (approximately 1/10 that of compensation inductors) and can often be neglected. To analyze the relationship between system efficiency and mutual inductance among multiple coils, incorporating the parasitic resistance of the compensating inductor and the coil, becomes extremely complex. To simplify the efficiency analysis while capturing the influence of mutual inductances, we initially neglect the parasitic resistances of the compensation inductors and coils. Following the approach for a four-coil system[31], we extend the analysis to a five-coil LCC-P system. Assuming identical transmitter coil structures, the compensation network parameters are unified as: L_r, C_r, C_p. Substituting Formulas (2) and (3) into Formula

(1) yields: I_n, I_{pn1}, I_{pn2}, I_s and other current expressions, we can calculate the system's input and output power expressions.

$$P_{out} = \frac{R_L D^2}{{L_r}^2 {L_s}^2 \omega^2} \tag{4}$$

$$P_{in} = \frac{R_L D^2 + jL_s \omega D^2 + j{L_s}^2 \omega \sum_{i=1}^{5} Uin_i S_i}{{L_r}^2 {L_s}^2 \omega^2} \tag{5}$$

where,

$$\begin{cases} D = M_1 Uin_1 + M_2 Uin_2 + M_3 Uin_3 + M_4 Uin_4 + M_5 Uin_5 \\ S = \sum_{j=1, j\neq i}^{5} M_{ij} Uin_j \end{cases} \tag{6}$$

According to Formulas (4) and (5), the system efficiency is obtained as

$$EFF = \frac{P_{out}}{P_{in}} = \frac{R_L D^2}{R_L D^2 + jL_s \omega D^2 + j{L_s}^2 \omega \sum_{i=1}^{5} Uin_i S_i} \tag{7}$$

Based on Formulas (4) and (7), if the system's compensation network and resonant frequency are fixed, the output power and efficiency of the five-coil system vary with changes in D and R_L. The same principle applies to any multi-input coil system.

If the compensation network of the system and the resonant frequency are determined, the output power and efficiency of the five-winding system will change with the variations of D and R_L. Similarly, it can be concluded that the results of any input coil network system are similar to those of the five-winding system.

Since the system is in resonance, the input voltage at resonance can be expanded as:

$$\begin{cases} Uin_1 = \frac{A_1}{\sqrt{2}} e^{j0} = \frac{A_1}{\sqrt{2}} \\ Uin_n = \frac{A_n}{\sqrt{2}} e^{j\theta_n} = \frac{A_n}{\sqrt{2}} (\cos\theta_n + j\sin\theta_n) \end{cases} \tag{8}$$

where, A_n is the amplitude and θ_n the phase angle of the nth input voltage relative to the first input.

When the UAV hovers within the charging zone, its battery load remains within a fixed range and cannot be altered. The position of the receiving coil is fixed, thereby determining the mutual inductances between the receiver and transmitters. Therefore, the system's output power and efficiency can only be adjusted by modifying the input voltages Uin_n, specifically their amplitude A_n and phases θ_n. Since the multi-input system is powered by a single source, control of Uin_n is implemented by adjusting the duty cycle and phase of the PWM signals driving the inverters.

Multi-input coil amplitude allocation strategy

According to Li et al.[32], under ideal conditions for optimal efficiency in a two-coil system, the relationship between current magnitudes is: $I_{p21} = xI_{p11}$, where $x = M_2/M_1$, Since the input employs an LCC compensation structure, the transmitter coil current is:

$$I_{pn1} = \frac{Uin_n}{j\omega Lr} \tag{9}$$

With constant compensation parameters, the current magnitude is linearly related to the input voltage. Hence, the optimal voltage ratio for two coils is:

$$Uin_2 = xUin_1 \tag{10}$$

According to Pang et al.[31], the condition for achieving optimal efficiency in a four-coil system with LCC-S compensation is the following relationship between the input current magnitude:

$$\begin{cases} I_{p21} = xI_{p11} \\ I_{p31} = yI_{p11} \\ I_{p41} = zI_{p11} \end{cases} \tag{11}$$

where, $x = M_2/M_1$, $y = M_3/M_1$, and $z = M_4/M_1$, similarly, in the LCC compensation structure, We have $Uin_2 = xUin_1$, $Uin_3 = yUin_1$, $Uin_4 = zUin_1$. Assuming that a similar structure exists in a five-coil system, let $Uin_5 = vUin_1$. in this system, the impedances of the input coil, the receiving coil, and the compensation inductor are considered. Substituting this parameter into the system efficiency formula will yield:

$$EFF = \frac{C_1 A^2}{C_2 B + C_3 A^2} \tag{12}$$

where, C_1, C_2, C_3 are related to L_s, ω, R_s, R_{rn}, R_{pn}, and $A = M_1 + M_2 x + M_3 y + M_4 z + M_5 v$, $B = 1 + x^2 + y^2 + z^2 + v^2$. To find the conditions for optimal efficiency, take the partial derivatives of x, y, z, v and set the derivatives equal to zero. By calculating the partial derivatives, we obtain:

$$\begin{cases} x = \frac{M_2}{M_1} \\ y = \frac{M_3}{M_1} \\ z = \frac{M_4}{M_1} \\ v = \frac{M_5}{M_1} \end{cases} \tag{13}$$

This indicates that, with fixed phases and system structure, optimal efficiency requires the input voltage amplitudes to be proportional to the respective mutual inductances. This conclusion holds for five-coil and general multi-coil structures.

Analysis of multi-input coil structure

The receiver coil size is determined by the UAV landing gear structure. Both transmitter and receiver coils are chosen as 20 × 20 cm squares. Simulations in ANSYS Electronics/Maxwell show that when all Tx coils are activated simultaneously, cross-coupling occurs among them. According to Formula (5), this increases the reactive power input to the system, degrading charging performance. As documented by Kang et al.[33], a specific lateral offset distance exists where cross coupling between two receiver coils becomes zero; a diagonal offset distance also eliminates cross coupling. However, in a four-coil configuration, overlapping cannot simultaneously nullify cross coupling for all four coils. Therefore, overlapping is used to minimize cross coupling as much as possible. Although overlapping reduces the effective charging area of the system compared to a non-overlapping configuration, it reduces the mutual inductance between adjacent Tx coils to nearly zero, significantly minimizing reactive circulating currents caused by cross-coupling. This enables the system to deliver more energy to the receiver, thereby improving system efficiency. Additionally, the overlapping coil configuration results in a more uniform magnetic field distribution, avoiding localized charging dead zones, which helps the UAV obtain relatively stable charging conditions at different landing positions. Maxwell simulations indicate that the zero cross-coupling lateral offset distance is 3.75 cm, which is selected as the spacing between adjacent transmitter coils for simulation and experimental testing.

Figure 4a, b displays the magnetic field distributions of four-coil and five-coil arrays, respectively. Analysis reveals that the four-coil array exhibits lower magnetic field strength at the center and significant field inhomogeneity, resulting in charging dead spots. Therefore, the five-coil array is selected for charging experiments. Figure 5 demonstrates how varying the phases of transmitter coil currents

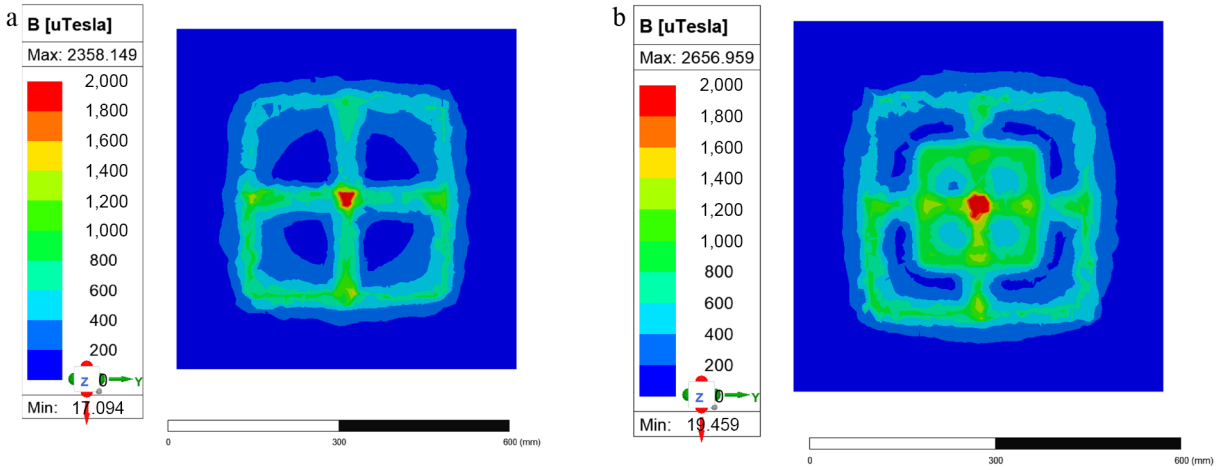


Fig. 4 (a) Simulation diagram of four-coil magnetic field strength. (b) Simulation diagram of five-coil magnetic field strength.

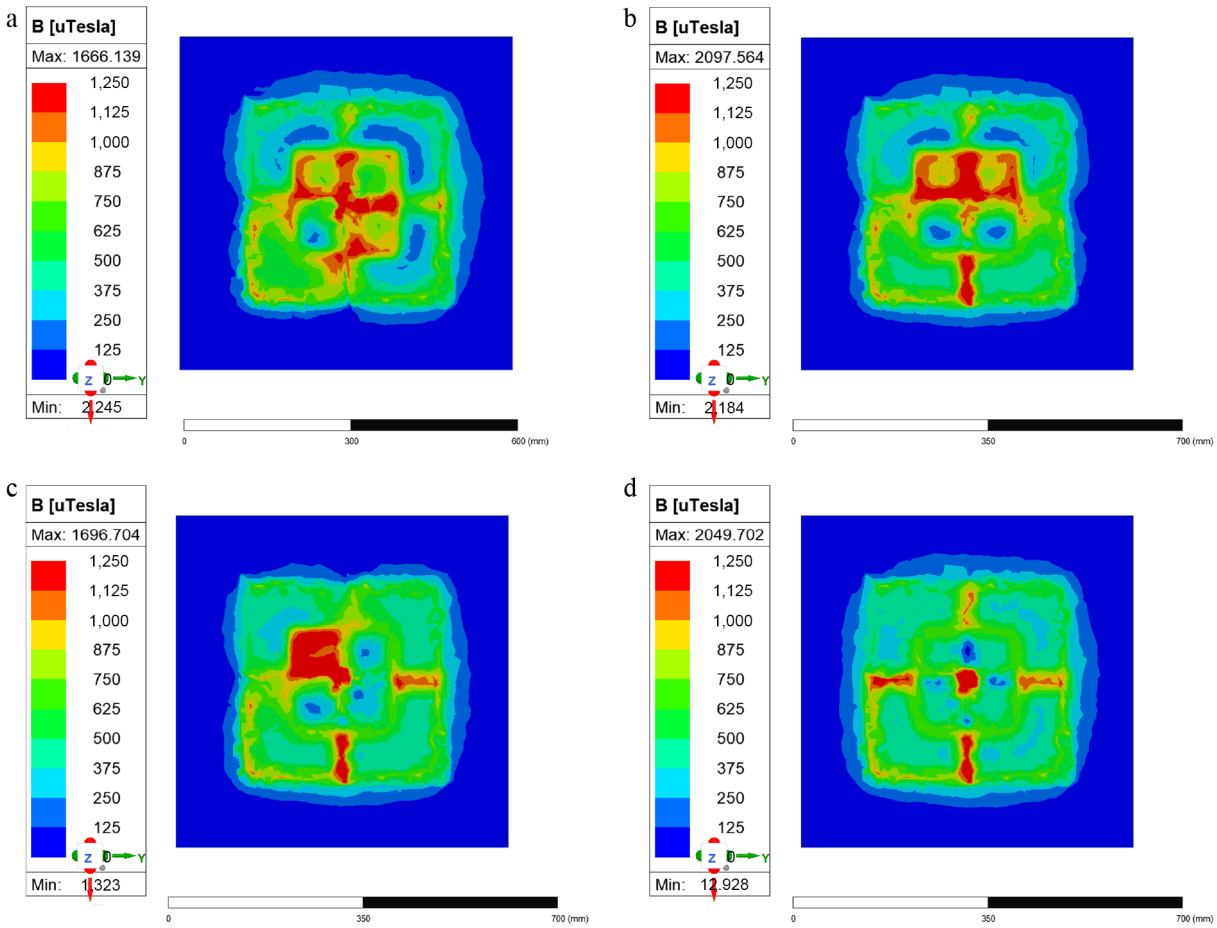


Fig. 5 (a) Tx1 is offset by 180°. (b) Tx1 and Tx2 are offset by 180°. (c) Tx1, Tx2, and Tx3 are offset by 180°. (d) Tx1, Tx2, Tx3, and Tx4 are offset by 180°.

can concentrate the magnetic field in specific regions. For example, Fig. 5b concentrates the field above Tx3, while Fig. 5c concentrates it at the junction of Tx3, Tx4, and Tx5. As shown in the figure above, analyzing the phase effect on the current in the receiving coil through the magnetic field angle is relatively challenging.

Figure 6 shows a comparison between the simulated mutual inductance values of the receiver coil and the five transmitter coils in the five-coil array (ANSYS Electronics/Maxwell) and the actual measured values. The simulation results closely match the experimental measurements. The simulation software can be used to model the mutual inductance values between the receiver coil and transmitter coils during an actual UAV landing and perform calculations.

Multi-input coil amplitude and phase optimization algorithm

The model indicates that all components in the MTA-WPT system are linear elements, and the system's transmitter source is unaffected by circuit devices. Therefore, it can be regarded as a

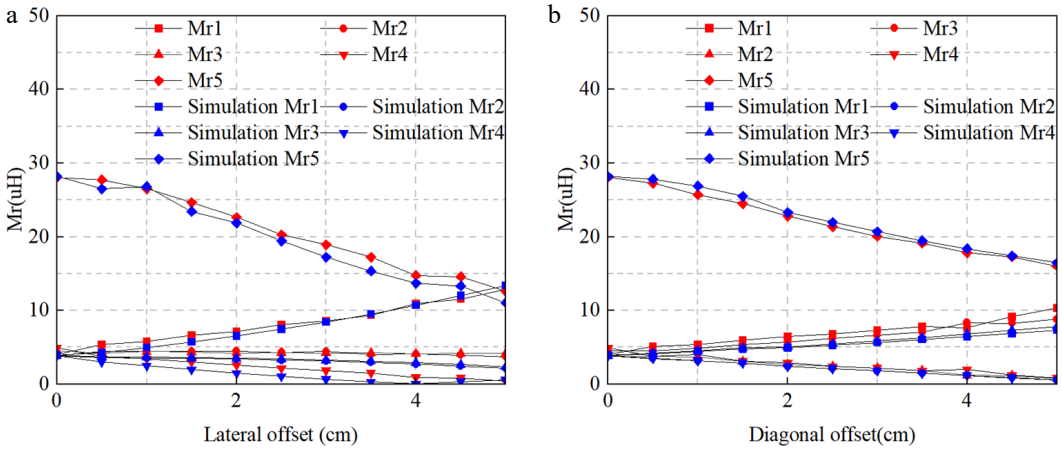


Fig. 6 The mutual inductance experiment and simulation results between the receiving coil and the five-antenna coil: (a) Lateral offset mutual inductance diagram, (b) diagonal offset mutual inductance diagram.

linear system and equivalently simplified into a multiport network model. This network retains only the input voltage source and receiving resistor, establishing the relationship between its input and output ports to better analyze the input-output response relationship.

According to Formula (8), it is evident that adjusting the phase of the input voltage can alter the overall system efficiency. For a multi-input single-output system, the relationship between the receiving-end voltage and the output-end voltage is given by:

$$I_L = \dot{A}_1 e^{j\dot{\theta}_1} + \dot{A}_2 e^{j\dot{\theta}_2} + \cdots + \dot{A}_n e^{j\dot{\theta}_n} \tag{14}$$

where, $\dot{A}_n$, and $\dot{\theta}_n$. represent the magnitude and phase of the received current at the load end generated by the nth transmitter. As shown in Formula (14), to maximize the received current, the phases of the received currents generated by the transmitters should be identical. At this point, the received current is a superposition of currents from each transmitter, influenced not only by the system's input voltage, the position and orientation of the transmitter and receiver coils, but also by the cross-coupling between transmitter coils. Therefore, when the phases of the received currents from different transmitters differ, two distinct phenomena may occur: destructive interference or constructive interference. To maintain maximum reception efficiency in a multi-coil system, we should adjust the phase of the input voltage to ensure the received current remains in a state of constructive interference as the mutual inductance between the receiving and transmitting coils varies.

Particle swarm optimization algorithm

This paper employs the PSO algorithm to determine maximum efficiency by adjusting the phase and amplitude of the system's input voltage. The algorithm updates the particle swarm using the following Formulas (15) and (16):

$$x_n(i) = x_n(i-1) + v_n(i) \tag{15}$$

$$\begin{aligned} v_n(i) = {} & w(i)v_n(i-1) + c_1 r_1[pbest_{n\max}(i-1) - \mathrm{x}_n(i-1)] \\ & + c_2 r_2[gbest_{\max}(i-1) - \mathrm{x}_n(i-1)] \end{aligned} \tag{16}$$

Among these, $x_n(i)$ represents the position variable of the nth particle in the i th iteration, $v_n(i)$ represents the velocity variable of the particle in the i th iteration, $pbest_{n\max}(i)$ is the individual optimal position of the nth particle in the i th iteration, and $gbest_{\max}(i)$ is the global optimal position in the i th iteration.c_1,c_2 are individual learning factors and group learning factors respectively, r_1, r_2 denote random numbers in the range of [0,1], $w(i)$ is the inertia weight factor of the system in the i-th iteration. The specific steps of the particle swarm optimization algorithm are shown in Fig. 7.

Analysis of algorithm parameters and their values

During algorithm execution, the inertia weight factor gradually decreases with each iteration to limit particle velocity and prevent them from getting stuck in local optima. When w < 0.8, the particle swarm algorithm exhibits local exploration capability, enabling it to find the global optimum solution at a relatively fast pace. Conversely, when w > 1.2, the algorithm demonstrates global search capability, allowing it to explore a broader search area. However, convergence speed slows down, potentially affecting the final search result. Therefore, this paper adopts the following formula for calculating the inertial weight:

$$w(i) = \max(0.4, 0.9w(i-1)) \tag{17}$$

From Formula (17), it can be seen that $w_{\max}$ = 0.9, $w_{\min}$ = 0.4. It can be observed that as the number of iterations gradually increases, it decreases linearly. This design ensures both strong global exploration capability in the early stages and effective local development capability in the later stages.

c_1 and c_2 are crucial parameters in the particle swarm optimization algorithm, as their values determine the global search performance and optimization efficiency. When the value of c_1 is low, the algorithm tends to search farther from the optimization target, whereas when the value of c_2 is high, the algorithm searches closer to the optimization target. To better counteract the uncertainty of the algorithm, the values of c_1 and c_2 are set to 1.5.

The optimization objective of this multi-coil model is constrained by the achievable output power of the system. Consequently, employing a penalty function to address constrained optimization is a common approach. This method transforms complex constraints into simpler unconstrained optimization problems by introducing a penalty term in the objective function. Solutions violating constraints incur penalties, and if the search direction contradicts the constraints, the penalty coefficient in the penalty function gradually increases. Solutions violating constraints incur progressively greater penalties, thereby gradually satisfying constraints during optimization.

From the above analysis, the primary physical constraints for this optimization are:

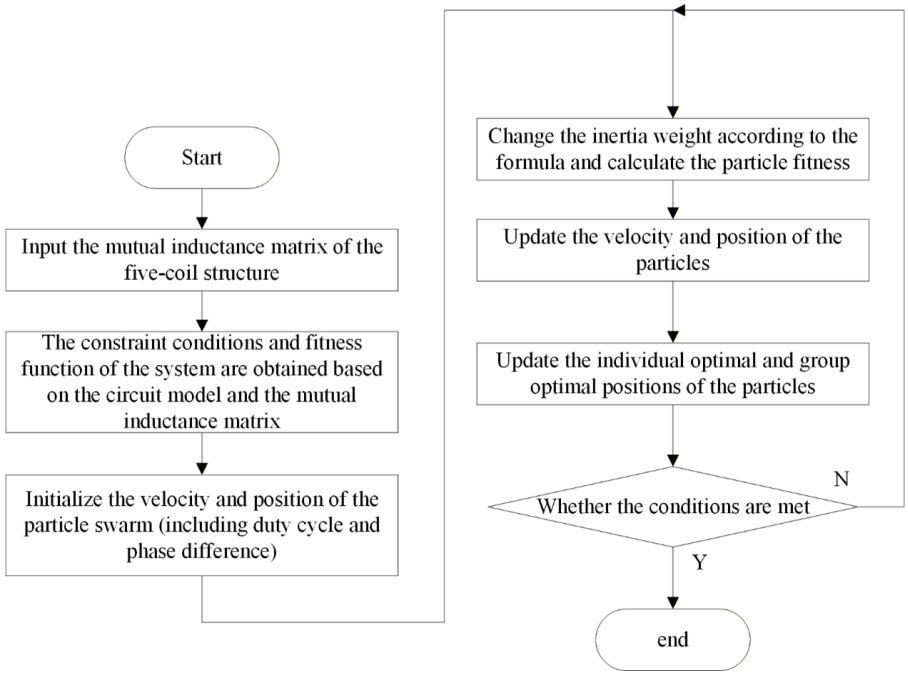


Fig. 7 Specific implementation steps of the particle swarm algorithm.

$$\begin{cases} Uin_n < \max_Uin \\ Pin_n > 0 \end{cases} \tag{18}$$

To handle the equality constraints in Formula (18), this paper adopts the exterior penalty function method. The basic idea is that when a search particle is outside the feasible region, a penalty term is introduced into the objective function. This penalty term increases sharply as the degree of constraint violation intensifies, thereby forcing the optimization process to approach the feasible region. Based on this, the fitness expression of the penalty function is:

$$F(x) = f(x) + \mu \mathrm{T}(x) \tag{19}$$

Therefore, the penalty function is defined as:

$$\begin{cases} f = f - penalty_1 \max(0, Uin_n - \max_Uin) \\ f = f - penalty_2 \max(0, 0 - Pin) \end{cases} \tag{20}$$

where, f is the fitness function, $penalty_1$ and $penalty_2$ are penalty coefficients set to 0.05 and 0.1, if the penalty coefficient is too large, the algorithm may prematurely abandon exploring potentially high-quality solutions near the boundary of the feasible region. Conversely, if the penalty coefficient is too small, the constraints may not be adequately satisfied. The current values ensure that the penalty for constraint violations accounts for approximately 10% to 30% of the total fitness, guaranteeing both the enforceability of the constraints and sufficient search space.

To ensure the system output power remains at a fixed value, a Gaussian function is employed to reward solutions closer to the target power. Specifically, solutions near the target power exhibit higher fitness, while those farther from the target power have lower fitness.

$$f_p = e^{-\left(\frac{P_{out} - T\arg et_power}{T\arg et_power}\right)^2} \tag{21}$$

While ensuring the output power, guarantee the efficiency of the system

$$f = h_1 f_p + h_2 f_{eff} \tag{22}$$

Here, f_p represents the system power fitness, f_{eff} denotes the system efficiency fitness, $T\arg et_power$ represents the target power, while h_1 and h_2 serve as the proportional coefficients corresponding to the fitness values.

Results

Experimental and simulation analysis of the optimal efficiency search algorithm for the MTA-WPT system

Experimental setup

To validate the theoretical analysis, a prototype five-transmitter-coil WPT system was built. The setup includes five inverters, five LCC compensation networks, five transmit coils, one receive coil, secondary compensation, and rectifiers. The inverters drive MOSFETs (FDH055N15A) via IR2104 controllers. The PWM signals are generated by an FPGA (xc7z020clg400-2), allowing adjustment of duty cycle and phase difference between inverters. The LCC compensation network uses PQ-2918 inductors and CCB capacitors. The receiver rectifier consists of four ES3B-E3/57T fast-recovery diodes. The system operates at a 24 V input and 100 kHz. Detailed parameters are listed in Table 1. The mutual inductance M matrix under the condition of 5 cm lateral offset is listed in Table 2, which shows the lateral offset in the x-axis. Here, $L_1 \sim L_5$ represent the self-inductances of the five transmitting coils, L_6 represents the self-inductance of the receiving coil, $M_1 \sim M_5$ represent the mutual inductances between each transmitting coil and the receiving coil, M_{ij} $(1 \le i \le 5,\ 1 \le j \le 5)$ represents the mutual inductance between the i-th transmitting coil and the j-th transmitting coil.The MTA-WPT system experimental prototype is shown in Fig. 8.

Experimental results

To verify that the experimental prototype can still achieve charging when the RX coil is in an offset position, the starting position was set with the RX coil centered within the five-coil array, with a Z-axis distance of 1 cm. When the input DC voltages were all set

Table 1. MTA-WPT system parameters.

Parameter	Experiment value	Parameter	Experiment value
Uin	24 V	L_s	37 μH
f	100 kHz	C_s	64.7 nF
L_r	15 μH	R_r	145 mΩ
C_r	163 nF	R_p	236 mΩ
C_p	110 nF	R_s	236 mΩ
L_p	37 μH	R_l	130 Ω

Table 2. The mutual inductance M matrix under the condition of a 5 cm lateral offset.

Self-inductance and mutual inductance	L_1	M_{12}	M_{13}	M_{14}	M_{15}	M_1
	M_{21}	L_2	M_{23}	M_{24}	M_{25}	M_2
	M_{31}	M_{32}	L_3	M_{34}	M_{35}	M_3
	M_{41}	M_{42}	M_{43}	L_4	M_{45}	M_4
	M_{51}	M_{52}	M_{53}	M_{54}	L_5	M_5
	M_1	M_2	M_3	M_4	M_5	L_6
Self-inductance and mutual inductance values	37.0863	0.621815	0.461625	1.866375	4.252525	10.3442
	0.621815	39.8564	2.363775	0.5875	4.2872	0.747275
	0.461625	2.363775	37.1706	0.439625	4.222975	8.8188
	1.866375	0.5875	0.439625	37.4132	4.6258	0.83975
	4.252525	4.2872	4.222975	4.6258	38.4432	16.01258
	10.3442	0.747275	8.8188	0.83975	16.01258	36.6945

to 24 V without amplitude or phase control, Output power was measured for the RX coil at horizontal offsets of 5 cm and diagonal offsets of 5 cm relative to the center position under various impedance conditions. Due to the symmetry of the multi-coil structure, experimental data were collected for only one direction of horizontal and diagonal offset. At a load impedance of 15 Ω, the maximum and minimum output powers were 71 and 36 W, respectively. Figure 9 shows that as the RX coil gradually deviates from the center—whether through horizontal or diagonal displacement—the system's output power progressively decreases with increasing displacement distance. To validate simulation accuracy, corresponding output power curves from Simulink simulations under various offset conditions are also presented. Since Simulink cannot simulate coil displacement, measurements of mutual inductance in the experimental coil array were used as input for the Simulink coupling structure. As shown in Fig. 9, the simulation data aligns closely with experimental results.

The voltage/current waveforms of the inverter, input coil, output coil, and load under a 5 cm lateral offset were measured using oscilloscopes ZDS5054Pro (ZLG) and DSOX3022T (Keysight), as shown in Figs 10–15.

To validate the system's constant current output performance, load current changes were captured using a PA323 power meter (ZLG), changes from 5 to 10, and then to 20 Ω. As shown in Fig. 16, the load current varied from 2.341 to 2.135 A. The current variation graph demonstrates that the system maintains near-constant load current during load changes.

Simulation and experimental analysis of the particle swarm optimization algorithm

Using Simulink software, a circuit model of the multi-coil coupled transmission system was constructed. The circuit parameters of the system are shown in Table 1. Through joint simulation with MATLAB

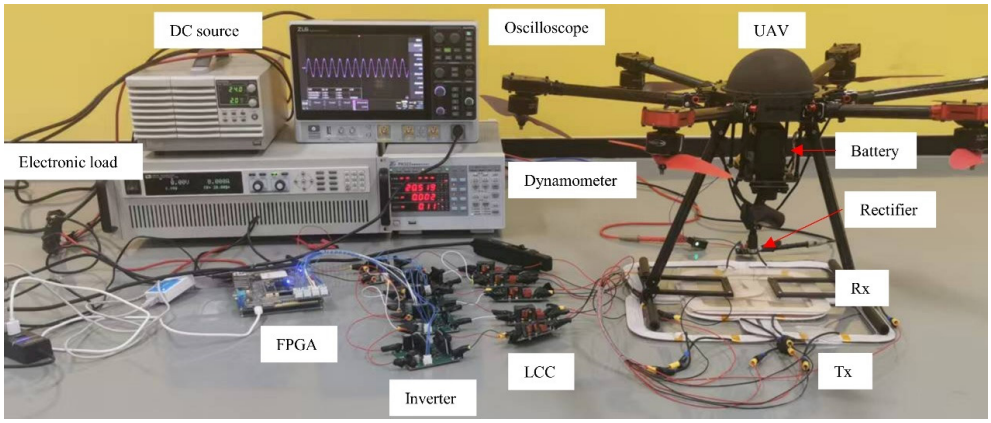


Fig. 8 MTA-WPT system experimental prototype.

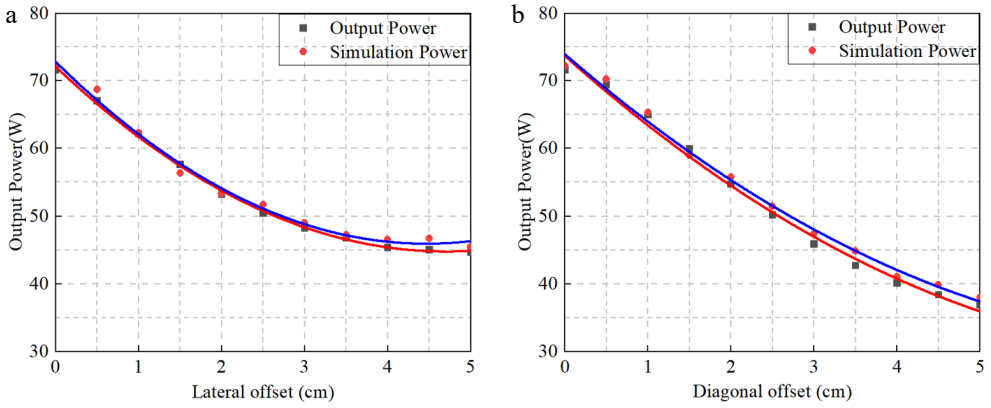


Fig. 9 Comparison of simulated and measured output power: (a) lateral offset; (b) diagonal offset.

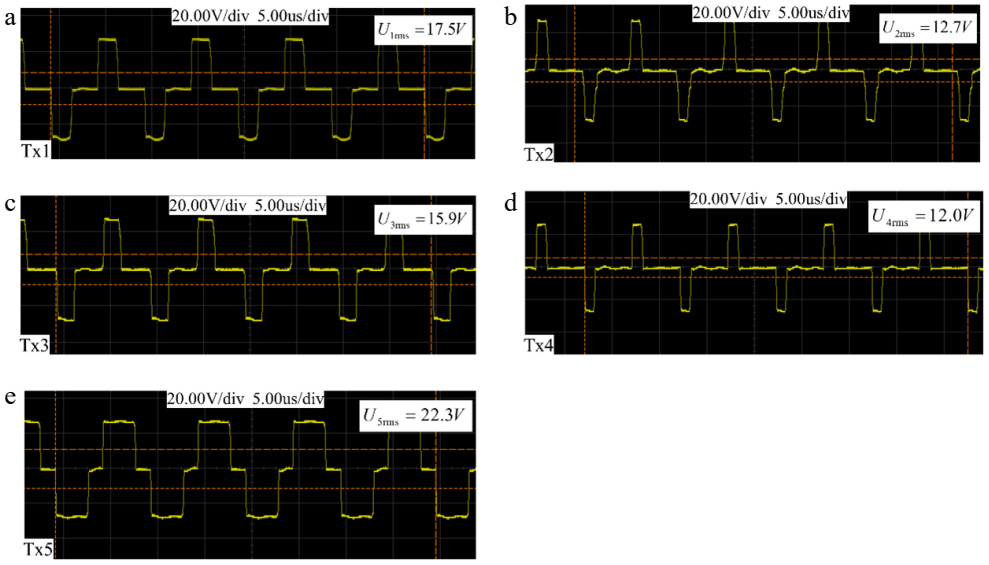


Fig. 10 Output voltages of the five-channel inverters. (a) Tx1. (b) Tx2. (c) Tx3. (d) Tx4. (e) Tx5.

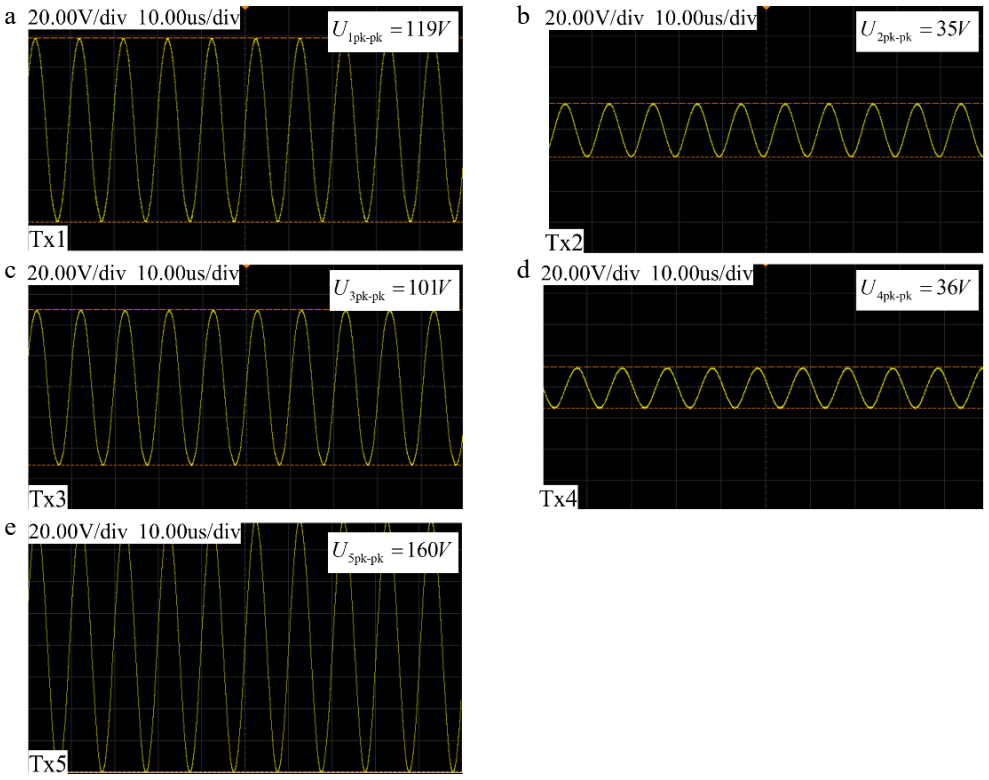


Fig. 11 Input voltage of the five-channel Tx coil. (a) Tx1. (b) Tx2. (c) Tx3. (d) Tx4. (e) Tx5.

and Simulink, the system's optimal efficiency under fixed power was optimized. With the default phase of Tx1 coil set to 0, the phase difference between each subsequent coil and its preceding coil was defined as its input variable. The respective inputs were: θ_{12}, θ_{23}, θ_{34}, θ_{45}. Therefore, the inputs for the particle swarm optimization algorithm were: θ_{12}, θ_{23}, θ_{34}, θ_{45}, and the duty cycle D_c. Here, D_c represents the duty cycle of the Tx1 coil. According to Formula (13), the input voltage amplitudes of the input system are proportionally distributed. Therefore, their duty cycles can also be expressed using mutual inductance ratios, thereby reducing the number of input variables in the system. After 20 runs, the average computation time of the PSO algorithm was 2 min 43 s, which is not long compared to the charging time and can meet the practical application requirements of the UAV system. The relevant parameters for the particle swarm optimization algorithm are shown in Table 3.

Similarly, with the RX coil centered in the four-coil array as the starting position, simulations were conducted to optimize output power and efficiency under different impedance conditions when the RX coil was horizontally offset by 5 cm and diagonally offset by 5 cm relative to the center position. This analysis compared power and efficiency with and without the search algorithm. The experimental results are shown in Fig. 17.

As shown in Fig. 17, Fig. 17a, b, under lateral displacement conditions, the algorithm maintains comparable charging efficiency to

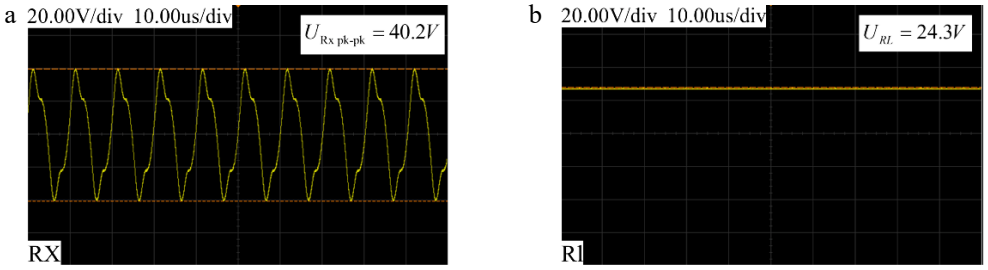


Fig. 12 (a) Output voltage of the Rx coil; (b) Input voltage of the load.

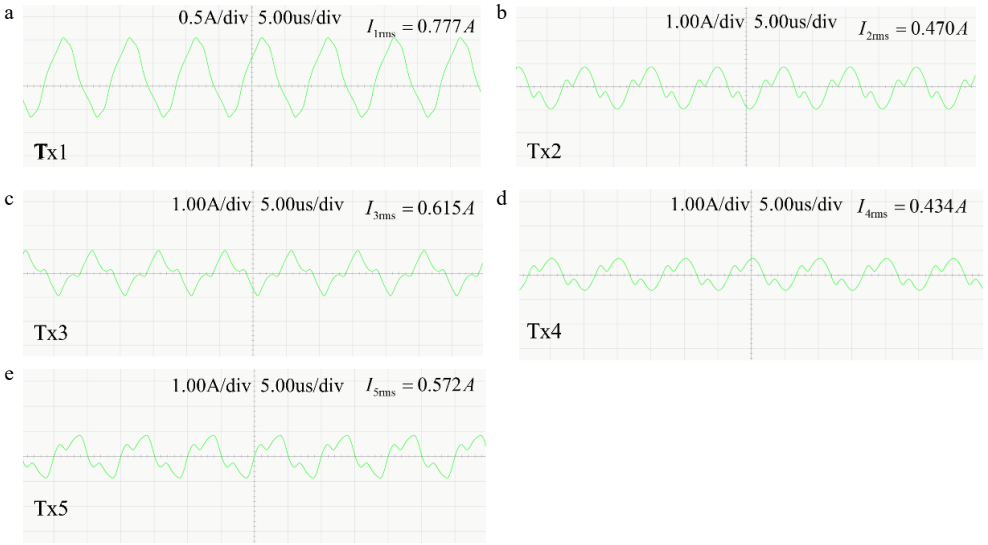


Fig. 13 Output currents of the five-channel inverters. (a) Tx1. (b) Tx2. (c) Tx3. (d) Tx4. (e) Tx5.

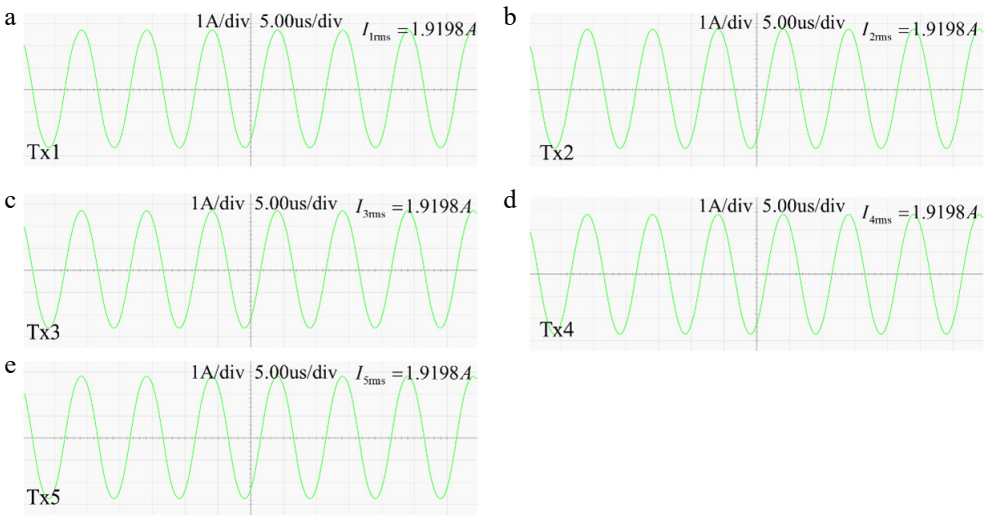


Fig. 14 Input currents of the five-channel Tx coil. (a) Tx1. (b) Tx2. (c) Tx3. (d) Tx4. (e) Tx5.

the non-algorithm approach during the initial displacement phase while maintaining stable power output. However, as displacement distance increases, the algorithm progressively enhances system efficiency. Fig. 17c, d illustrates diagonal displacement scenarios. Under stable-power conditions, the algorithm significantly enhances system efficiency across the entire displacement range. For a load of 20 Ω, lateral displacement of 5 cm, and charging power of 30 W, system efficiency peaks at 72.51%, up from 67.69%, representing an increase of 4.82%. This demonstrates that the optimized algorithm achieves superior efficiency compared to the unoptimized algorithm at the set power level by adjusting phase and amplitude. Tables 4 and 5 present the efficiency data as the offset distance increases.

UAV constant current charging experiment

To validate the charging performance of the UAV battery, charging experiments were conducted. The battery pack has a full voltage of 22.2 V. Wireless charging input was set to 32 V to achieve 1.5 A constant current and charging at approximately 30 W. The UAV was positioned at the center, with a lateral offset of 5 cm, and

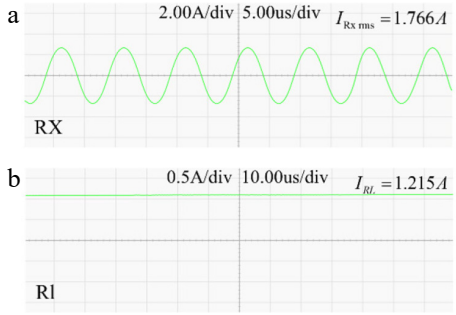


Fig. 15 (a) Output current of the Rx coil; (b) Input current of the load.

with a diagonal offset of 5 cm for charging tests. The charging voltage and current at a diagonal offset of 5 cm are shown in Fig. 18.

During the 46-min charging cycle with a 5 cm diagonal offset, the charging current remained essentially constant at approximately 1.5 A. The battery voltage increased from 20 to 21 V, with charging power maintaining around 30 W. This demonstrates that even with system displacement, the LCC-P topology enables the system to maintain a constant charging current. Consequently, charging curves at other system positions exhibit similar characteristics to those shown in Fig. 18.

As shown in Figs 19–21, the algorithm slightly improves system efficiency when the receiver coil is centered. However, when the receiver coil is significantly offset from the center, system efficiency increases substantially-a result consistent with electronic load experiments. At a charging power of approximately 30 W,

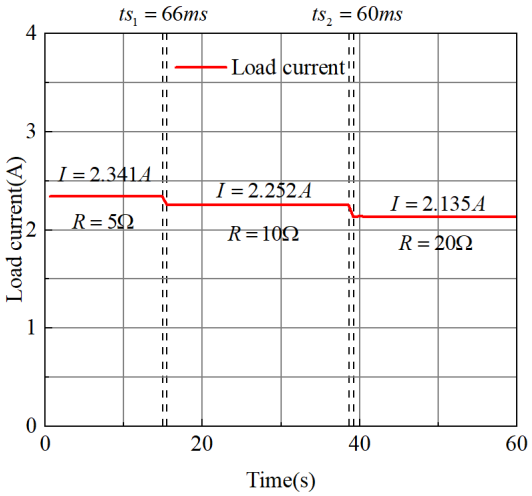


Fig. 16 The load current varies with the load.

maximum efficiency rose from 57.56% to 67.72%, representing a 10.16% improvement. In summary, the system employs a multi-transmitter coil configuration with the algorithm to achieve high-efficiency charging of UAV batteries.

Further discussion and prospects

To determine the position information of the UAV, the following scheme can be applied to the MTA-WPT system. Based on the different positions of the receiving coil, the phase of the input current

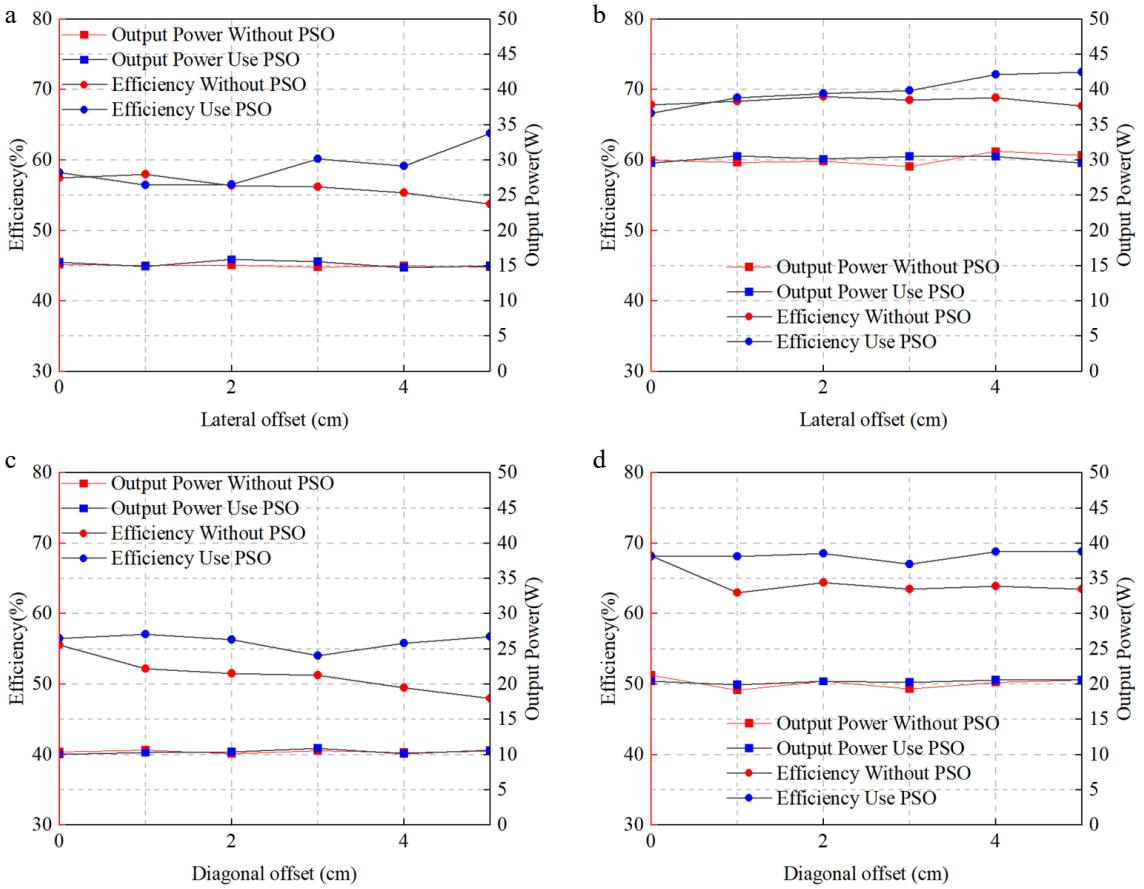


Fig. 17 (a) Efficiency curve at 15 W with 10 Ω Load and 5 cm horizontal offset. (b) Efficiency curve at 30 W with 20 Ω load and 5 cm horizontal offset. (c) Efficiency curve at 10 W with 10 Ω load and 5 cm diagonal offset. (d) Efficiency curve at 20 W with 20 Ω Load and 5 cm diagonal offset.

Table 3. Algorithm parameter settings.

Parameter	Parameter value
Position variables (including four phase differences and duty ratios)	−90°~90°; 0.05~0.5
Number of particles N	50
Number of iterations iter	100
Speed variable v	−5~5; −0.02~0.02
Inertia weight w	0.4~0.9
Learning factor c_1, c_2	1.5
Proportional coefficient h_1, h_2	0.75, 0.25
Penalty coefficient $penalty_1$, $penalty_2$	0.05, 0.1

Table 4. Efficiency comparison under horizontal offset.

Offset distance (cm)	Efficiency without PSO for 10 Ω (%)	Efficiency use PSO for 10 Ω (%)	Efficiency without PSO for 20 Ω (%)	Efficiency use PSO for 20 Ω (%)
0	57.4933	58.23086	67.85213	66.66081
1	57.989	56.47121	68.33018	68.84291
2	56.35397	56.53843	69.02037	69.42831
3	56.19405	60.18519	68.50459	69.87048
4	55.33274	59.14359	68.86572	72.12933
5	53.75083	63.80204	67.68607	72.51287
Output power (W)	15	15	30	30

Table 5. Efficiency comparison under diagonal offset.

Offset distance (cm)	Efficiency without PSO for 10 Ω (%)	Efficiency use PSO for 10 Ω (%)	Efficiency without PSO for 20 Ω (%)	Efficiency use PSO for 20 Ω (%)
0	55.59878	56.5317	68.22239	68.14133
1	52.20701	57.12194	62.98619	68.1694
2	51.52683	56.29865	64.40019	68.58894
3	51.25058	54.06424	63.50154	67.0334
4	49.53487	55.81579	63.8911	68.78317
5	48.01168	56.78205	63.4688	68.78317
Output power (W)	10	10	20	20

I_{pn1} in each transmitting coil branch varies. If the receiving coil is positioned exactly at the center of the transmitting coil, the phase difference between the branch current I_{pn1} of each transmitting coil and the input voltage Uin_n is zero. As the receiving coil deviates further from the center of the transmitting coil, the phase difference between the branch current I_{pn1} and the input voltage Uin_n becomes more pronounced. Therefore, by collecting the branch currents I_{pn1} of each transmitting coil and determining their phase differences with the input voltage Uin_n, the mutual inductance relationship between the receiving coil and the transmitting coils under the current state can be identified, thereby obtaining the position information of the UAV.

Conclusions

This study investigates the charging efficiency and power output of a UAV landing at different positions within a multi-transmitter coil array. Experimental results demonstrate that the amplitude and phase allocation strategy optimized by the proposed Particle Swarm Optimization (PSO) algorithm can effectively improve the system efficiency under UAV landing misalignment conditions. Specifically, with a 20 Ω electronic load, the PSO algorithm achieves a maximum efficiency of 72.51%. When charging a UAV battery at approximately 30 W, system efficiency improves by 10.16% compared to operation without algorithm control, reaching 67.72%. Overall, the experimental results verify that this method provides a reliable solution for the stable wireless charging of UAVs under landing misalignment conditions.

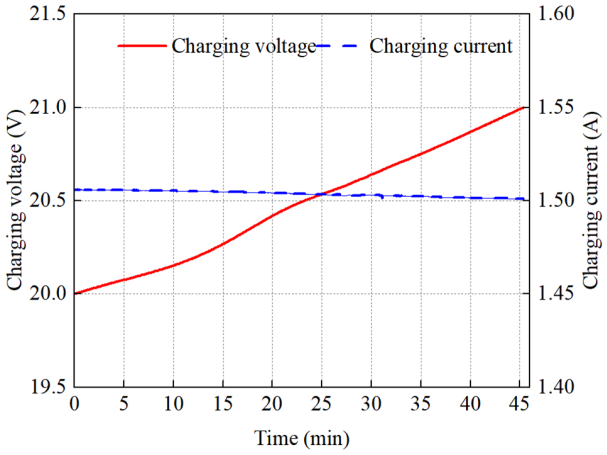


Fig. 18 The charging voltage and current under a 5 cm diagonal offset.

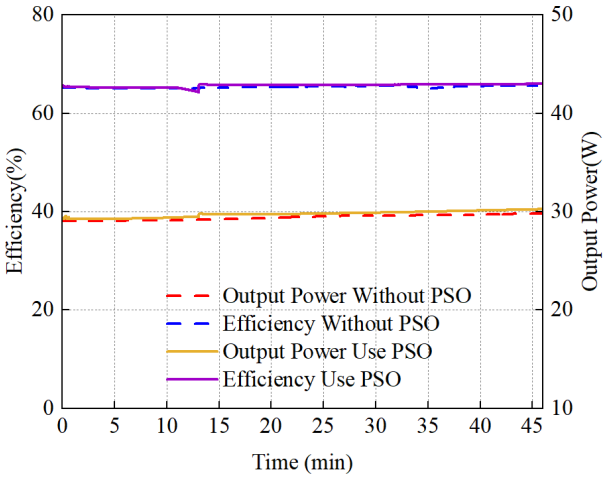


Fig. 19 Charging power and efficiency diagram of the receiving coil at the center of the coil array.

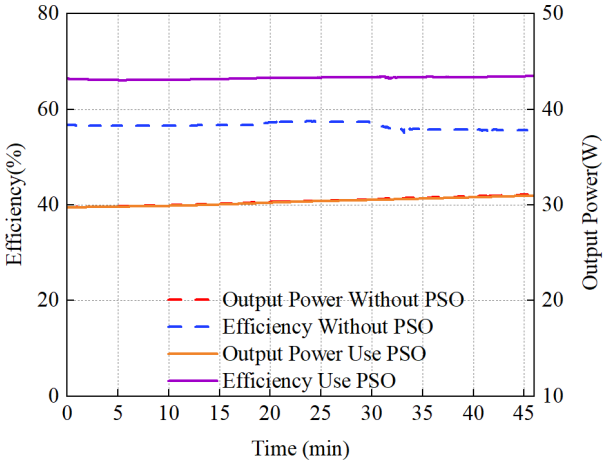


Fig. 20 Charging power and efficiency graph with the transverse offset of the receiving coil by 5 cm.

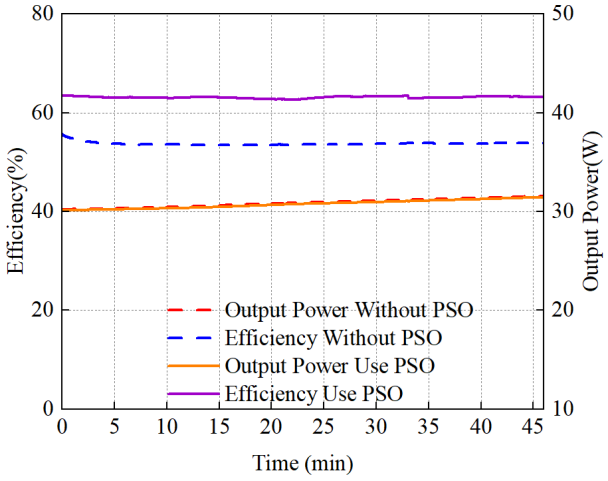


Fig. 21 Graph showing the charging power and efficiency when the diagonal offset of the receiving coil is 5 cm.

Author contributions

The authors confirm their contributions to the paper as follows: study conception and design: Zhang Y, Liu Y, Xu J, Pang S; data collection: Liu Y, Li C, Yang S; analysis and interpretation of results: Yang Y, Liu Y, Xu J, Pang S; draft manuscript preparation: Liu Y, Xu J, Pang S, Li H. All authors reviewed the results and approved the final version of the manuscript.

Data availability

The datasets generated during and/or analyzed in the current study are available from the corresponding author upon reasonable request.

Acknowledgments

This work was supported in part by the National Science Foundation of China (Grant No. 62503355), in part by the Postdoctoral Fellowship Program of CPSF (Grant No. GZB20250851), in part by the Tianjin Natural Science Foundation (Grant No. 25JCQNJC01940), in part by the Young Elite Scientist Sponsorship Program by Cast (Grant No. YESS20230630), and in part by the National Science and Technology Major Project of China (Grant No. ZDZX20250104).

Conflict of interest

The authors declare that they have no conflict of interest.

Dates

Received 14 January 2026; Revised 29 April 2026; Accepted 6 May 2026; Published online 28 October 2026

References

[1] Zhang Z, Pang H, Georgiadis A, Cecati C. 2019. Wireless power transfer — an overview. *IEEE Transactions on Industrial Electronics* 66(2):1044–1058

[2] Nguyen BX, Peng W, Vilathgamuwa DM. 2016. An overview of power circuit topologies for inductive power transfer systems. *2016 IEEE International Conference on Sustainable Energy Technologies (ICSET), Hanoi, Vietnam, 14–16 November, 2016*. USA: IEEE. pp. 256–263 doi: 10.1109/ICSET.2016.7811792

[3] Chu SY, Cui X, Zan X, Avestruz AT. 2022. Transfer-power measurement using a non-contact method for fair and accurate metering of wireless power transfer in electric vehicles. *IEEE Transactions on Power Electronics* 37(2):1244–1271

[4] Sagar A, Kashyap A, Nasab MA, Padmanaban S, Bertoluzzo M, et al. 2023. A comprehensive review of the recent development of wireless power transfer technologies for electric vehicle charging systems. *IEEE Access* 11:83703–83751

[5] Barmada S, Musolino A, Zhu J, Yang S. 2023. A novel coil architecture for interoperability and tolerance to misalignment in electric vehicle WPT. *IEEE Transactions on Magnetics* 59(5):1–5

[6] Xu J, Li X, Li H, Xie Z, Ma Q. 2022. Maximum efficiency tracking for multitransmitter multireceiver wireless power transfer system on the submerged buoy. *IEEE Transactions on Industrial Electronics* 69(2):1909–1919

[7] Xu J, Li X, Xie Z, Fu C, Du R. 2020. Design and analysis of inductively coupled power transfer system on mooring buoy with double ultracapacitor chargers using indirect control. *IEEE Transactions on Industrial Electronics* 67(6):4836–4845

[8] Guo K, Zhou J, Sun H, Yao P. 2019. Design considerations for a position-adaptive contactless underwater power deliver system. *2019 22nd International Conference on Electrical Machines and Systems (ICEMS), Harbin, China, 11–14 August, 2019*. USA: IEEE. pp. 1–6 doi: 10.1109/ICEMS.2019.8922503

[9] Wu M, Su L, Chen J, Duan X, Wu D, et al. 2022. Development and prospect of wireless power transfer technology used to power unmanned aerial vehicle. *Electronics* 11(15):2297

[10] Gu Y, Wang J, Liang Z, Zhang Z. 2022. Mutual-inductance-dynamic-predicted constant current control of LCC-P compensation network for drone wireless in-flight charging. *IEEE Transactions on Industrial Electronics* 69(12):12710–12719

[11] Li Z, He J, Huo Y, Ban M, Liu Y, et al. 2023. High-misalignment tolerance and output adjustable wireless charging system *via* detuned series–series compensated reconfigurable transmission channels. *IEEE Transactions on Power Electronics* 38(10):11786–11801

[12] Zhao Y, Shen S, Yin F, Wang L. 2025. A high misalignment-tolerant hybrid coupler for unmanned aerial vehicle WPT charging systems. *IEEE Transactions on Transportation Electrification* 11(1):1570–1581

[13] Yu L, Wu L, Zhu Y, Cao X, Zhang G, et al. 2022. Wireless charging concave coil design for UAVs. *Electronics* 11(13):1962

[14] Dong S, Jiao Z, Sun X, Liu X. 2016. Dynamic allocation algorithm for the gain of UAV nose wheel steering and differential braking based on decomposition control. *2016 IEEE International Conference on Aircraft Utility Systems (AUS), Beijing, China, 10–12 October*, 2016. USA: IEEE. pp. 831–835 doi: 10.1109/AUS.2016.7748168

[15] Wang Q, Li X, Yang F, Gao T. 2023. UAV-WPT system based on novel magnetic structure and model predictive control. *Sensors* 23(15):6859

[16] Nguyen BX, Vilathgamuwa DM, Foo GHB, Wang P, Ong A, et al. 2015. An efficiency optimization scheme for bidirectional inductive power transfer systems. *IEEE Transactions on Power Electronics* 30(11):6310–6319

[17] Pang H, Chau KT, Han W, Liu W, Zhang Z. 2022. Decoupled-double D coils based dual-resonating-frequency compensation topology for wireless power transfer. *IEEE Transactions on Magnetics* 58(2):8000407

[18] Jiang Y, Wang L, Wang Y, Wu M, Zeng Z, et al. 2020. Phase-locked loop combined with chained trigger mode used for impedance matching in wireless high power transfer. *IEEE Transactions on Power Electronics* 35(4):4272–4285

[19] Bie Z, Zhang J, Song K, Wang DA, Zhu C. 2022. A free-rotation asymmetric magnetic coupling structure of UAV wireless charging platform with conformal pickup. *IEEE Transactions on Industrial Electronics* 69(10):10154–10161

[20] Le-Huu H, Seo C. 2021. Dual-band free-positioning transmitting coil for multiple-receiver wireless power transfer. *IEEE Access* 9:107298–107308

[21] Shi Z, Sun Q, Wang J, Liu Z. 2024. Free-position dynamic WPT system supporting in-flight concurrent charging for multiple unmanned aerial vehicles. *IEEE Transactions on Power Electronics* 39(12):15389–15397

[22] Jeon SJ, Seo DW. 2022. Effect of additional transmitting coils on transfer distance in multiple-transmitter wireless power transfer system. *IEEE Access* 10:9174–9183

[23] Zeng Y, Sun Y, Zheng K, Li Z, Gao J, et al. 2025. An anti-misalignment and reconfigurable wireless power transfer system using bipolar coil array for autonomous underwater vehicles. *2025 10th Asia Conference on Power and Electrical Engineering (ACPEE), Beijing, China, 15–19 April, 2025*. USA: IEEE. pp. 875–879 doi: 10.1109/ACPEE64358.2025.11040186

[24] Yoon S, Lim T, Lee Y. 2024. Coil array technique with maximum tolerance to 2-D misalignment for wireless power transfer systems. *IEEE Transactions on Microwave Theory and Techniques* 72(6):3819–3828

[25] Covic GA, Kissin MLG, Kacprzak D, Clausen N, Hao H. 2011. A bipolar primary pad topology for EV stationary charging and highway power by inductive coupling. *2011 IEEE Energy Conversion Congress and Exposition, Phoenix, AZ, USA, 17–22 September, 2011*. USA: IEEE. pp. 1832–1838 doi: 10.1109/ECCE.2011.6064008

[26] Matsuura K, Ishihara M, Konishi A, Umetani K, Hiraki E. 2020. Multiple-transmitter achieving load-independent transmitter current and compensation of cross-interference among transmitters for wide charging area wireless power transfer systems. *2020 IEEE Energy Conversion Congress and Exposition (ECCE), Detroit, MI, USA, 11–15 October, 2020*. USA: IEEE. pp. 5474–5481 doi: 10.1109/ECCE44975.2020.9235430

[27] Huh S, Ahn D. 2018. Two-transmitter wireless power transfer with optimal activation and current selection of transmitters. *IEEE Transactions on Power Electronics* 33(6):4957–4967

[28] Wen F, Zhang X, Li Q, Wang L, Ma J, et al. 2023. Coil optimization and power orientation strategy of wireless power transfer system based on array coils. *Energy Reports* 9:781–789

[29] Oh MJ, Danuor P, Jung YB. 2023. A study on the optimal magnetic beam forming of coil arrays for long distance wireless power transmission. *Sensors* 23(11):5312

[30] Liu Y, Al Mahmud SA, Ha-Van N, Jayathurathnage P, Kyyrä J, et al. 2024. Noncoherent power combining for free-positioning wireless power transfer in large area. *IEEE Transactions on Industrial Electronics* 71(11):13980–13990

[31] Pang S, Xu J, Xie Z, Lu J, Li H, et al. 2023. Lightweight UAV's wireless power transfer system for constant current charging without secondary feedback control. *IEEE Transactions on Vehicular Technology* 72(12):15611–15621

[32] Li X, Sun B, Xu J, Pang S, Li H. 2023. Design and analysis of misalignment insensitive wireless power transfer system based on multitransmitter for constant power. *IEEE Journal of Emerging and Selected Topics in Power Electronics* 11(4):4536–4548

[33] Kang N, Shao Y, Liu M, Ma C. 2022. Analysis and implementation of 3D magnetic field shaping *via* a 2D planar transmitting coil array. *IEEE Transactions on Power Electronics* 37(1):1172–1184

Copyright: © 2026 by the author(s). Published by Maximum Academic Press, Fayetteville, GA. This article is an open access article distributed under Creative Commons Attribution License (CC BY 4.0), visit https://creativecommons.org/licenses/by/4.0/.